AGU PUBLICATIONS

Water Resources Research

RESEARCH ARTICLE

10.1002/2013WR014906

Key Points:

- Improved flood model formulation
- Comparative performance study
- Implication to flood modeling practice

Correspondence to:
G. Kesserwani,
g.kesserwani@shef.ac.uk

Citation:
Kesserwani, G., and Y. Wang (2014), Discontinuous Galerkin flood model formulation: Luxury or necessity?, *Water Resour. Res.*, *50*, 6522–6541, doi:10.1002/2013WR014906.

Received 15 OCT 2013
Accepted 19 JUL 2014
Accepted article online 24 JUL 2014
Published online 13 AUG 2014

Discontinuous Galerkin flood model formulation: Luxury or necessity?

Georges Kesserwani[1] and Yueling Wang[2]

[1]Pennine Water Group, Department of Civil and Structural Engineering, University of Sheffield, Sheffield, UK, [2]Key Laboratory of Water Cycle and Related Land Surface Processes, Institute of Geographic Sciences and Natural Resources Research, Chinese Academy of Sciences, Beijing, China

Abstract The finite volume Godunov-type flood model formulation is the most comprehensive amongst those currently employed for flood risk modeling. The local Discontinuous Galerkin method constitutes a more complex, rigorous, and extended local Godunov-type formulation. However, the practical merit associated with such an increase in the level of complexity of the formulation is yet to be decided. This work makes the case for a second-order Runge-Kutta Discontinuous Galerkin (RKDG2) formulation and contrasts it with the equivalently accurate finite volume (MUSCL) formulation, both of which solve the Shallow Water Equations (SWE) in two space dimensions. The numerical complexity of both formulations are presented and their capabilities are explored for wide-ranging diagnostic and real-scale tests, incorporating all challenging features relevant to flood inundation modeling. Our findings reveal that the extra complexity associated with the RKDG2 model pays off by providing higher-quality solution behavior on very coarse meshes and improved velocity predictions. The practical implication of this is that improved accuracy for flood modeling simulations will result when terrain data are limited or of a low resolution.

1. Introduction

The development of hydraulic modeling tools to predict flood inundation has undergone significant progress over the past few decades. Most of these models are based on the explicit numerical solution of the depth-averaged shallow water equations (SWE) representing the principles of mass and momentum conservation of water in two horizontal dimensions. Several types of modeling techniques have been adopted, each considering different levels of physical and/or numerical complexity for the model's formulation. Useful studies surveying the merits and limitations of different, popular model formulations include the papers of *Néelz and Pender* [2013], *Neal et al*. [2012], and *Almeida and Bates* [2013]. The current study elaborates further on the finite volume Godunov-type formulation, which is by far the most comprehensive and incorporates the widest range of flow transitions [*Toro and García-Navarro*, 2007]. It addresses the question of whether an even more complex formulation, i.e., the Discontinuous Galerkin (DG) formulation, would have practical merit in the field of flood inundation modeling.

A Godunov-type formulation may be thought of as a conservative finite volume numerical method that further adds in the physics of nonlinear wave propagation [*Godunov*, 1959; *Toro* 2001; *Guinot*, 2003]. The starting point is to write the SWE in a conservative integral form expressing the spatial flux as function of the state variables. With a local finite volume approximation, flow variables are averaged as piecewise-constant data per discrete element but with inter-elemental discontinuities. These nonlinear discontinuities are soundly communicated by means of the solutions of the Riemann problem during the calculation of spatial fluxes [*Toro and García-Navarro*, 2007]. In its basic form, the Godunov-type formulation is inherently local and first-order accurate, but the philosophy has been used to design higher-order variants with increased level of accuracy but at the price of losing the locality of the calculation stencil [e.g., *Van Leer*, 1979; *Caleffi et al*., 2007]. This may be a key reason why usable Godunov-type model are frequently first-order accurate [*Lhomme et al*., 2010; *Neal et al*., 2012].

In the applied context, Godunov-based hydraulic models have received many improvements, lending themselves to real-scale flood forecasting [e.g., *Liang*, 2010; *Gallegos et al*., 2009; *Sanders et al*., 2010; *Crossley et al*., 2010] and related problems [e.g., *George and LeVeque*, 2006; *Li and Duffy*, 2011; *Li et al*., 2013; *Murillo* *and García-Navarro*, 2012; *Morales-Hernández et al*., 2013; *Volp et al*., 2013]. Particular improvements include: (i) second-order accurate extensions achieved by the (nonlocal) MUSCL linear interpolation approach [e.g., *Aureli et al*., 2008; *Wang et al*., 2011], (ii) accurate integration of topographic gradient terms [e.g., *Bradford and Sanders*, 2002; *Audusse et al*., 2004; *Benkhaldoun et al*., 2010; *LeFloch and Tanh*, 2011; *Guan et al*., 2013], and (iii) the conservative modeling of moving wet/dry fronts with stable treatment of high roughness terms [e.g., *Nikolos and Delis*, 2009; *Liang and Marche*, 2009; *Mungkasi and Roberts*, 2010]. A Godunov-type hydraulic model that possesses features (i)–(iii) may be considered to be the most accurate and complex formulation that is currently used for food risk modeling.

More recently, with the emergence of the Discontinuous Galerkin (DG) method, a *local* Godunov-type formulation *with arbitrary order of accuracy* may be intrinsically derived for the SWE providing thereby an even more complex and sophisticated formulation than the finite volume framework [e.g., *Kesserwani and Liang*, 2010]. The DG method makes greater use of finite element theory to give a *local* polynomial solution that is invariantly compact and genuinely discontinuous. This provides an approximation mechanism to locally scale accuracy-order and, more importantly, to readily conserve the inter-element flux calculation featuring in Godunov-type methods [*Cockburn and Shu*, 2001]. However, the DG formulation requires storing and evolving more than one local averaged coefficient datum to define a local polynomial solution [*Zhou et al*., 2001]. The number of coefficients needed depends on the accuracy-order and the spatial dimensionality. Proportional to these factors, the complexity of the local DG formulation increases and, moving to too high an order would compromise the enhanced computational efficiency and make it more difficult to incorporate important practical features such as the inclusion of topographic gradients and wetting/drying fronts, discussed above. Consequently, a second-order local DG flood model formulation may be a balanced choice for applied shallow water hydrodynamics.

In theory, second-order DG methods have become quite developed for modeling shallow water flows. They are receiving increasing interest in water resource research in light of the applied advances adopted in finite volume methods [e.g., *Bokhove*, 2005; *Ern et al*., 2008; *Gourgue et al*., 2009; *Kesserwani and Liang*, 2012a]. In addition to the factors discussed above under (ii) and (iii), these also include other characteristic features such as *hp*-adaptivity, local slope coefficient limiting, polynomial wet/dry front tracking, and the time stepping issue [e.g., *Krivodonova et al*., 2004; *Kubatko et al*., 2009; *Kesserwani and Liang*, 2011, 2012b; *Xing et al*., 2010; *Araud et al*., 2012]. However, the DG formulation is seldom adopted for the simulation of flood propagation problems hindered, perhaps, by its excessive complexity. It is therefore of vital importance to uncover its main capabilities and limitations pertaining to the practice of flood inundation modeling and relative to the traditional finite volume Godunov-type formulation. This will be the aim of this paper, which is organized as follows.

First, the two-dimensional (2-D) SWE physical model is presented. Second, the technical details of a second-order DG flood model formulation (i.e., RKDG2) and an equally accurate finite volume formulation (i.e., MUSCL), both solving the SWE, are described. Both formulations are implemented with the same time integration scheme, same nonlinear slope limiter function, and same approaches to incorporating the necessary practical features described above (see (ii) and (iii)). However, we provide particular insights on the differences between them in terms of level of numerical complexity. Third, selected test cases are used to illustrate the most relevant behavior of the solutions obtained with the two formulations. These include the ability to capture flow transitions, mesh convergence, smooth flow curvature and the ability to handle irregular terrain by wetting and drying, and friction effects. Preliminary diagnostic testing is done to identify and contrast general behavioral differences between the local DG formulation and the finite volume counterpart. The local DG formulation is then assessed in modeling two real-scale scenarios featured in torrential and fluvial flood propagation events. Finally, the findings are summarized and key conclusions are outlined.

2. Depth-Averaged Shallow Water Equations (SWE)

The two-dimensional (2-D) depth-averaged SWE may be written in the following conservative form [e.g., *Liang*, 2010]:

$$\partial_t \mathbf{U} + \partial_x \mathbf{F}(\mathbf{U}) + \partial_y \mathbf{G}(\mathbf{U}) = \mathbf{S}(\mathbf{U}) \tag{1}$$

where (x,y) are the Cartesian coordinates, *t* is the time, $\mathbf{U}=[\eta, hu, hv]^{\mathrm{T}}$ is the flow vector in which $\eta = h + z$ represents the free-surface elevation, with $h(x, y, t)$ is the water level and $z(x, y)$ is the topography function, and $hu(x,y,t)$ and $hv(x,y,t)$ are the Cartesian components of unit-width discharge; $\mathbf{F}=[hu,(hu)^2/h+0.5g(\eta^2-2z\eta),huv]^{\mathrm{T}}$ and $\mathbf{G}=[hv,huv,(hv)^2/h+0.5g(\eta^2-2\eta z)]^{\mathrm{T}}$ are flux vectors relative to the x and y directions, in which the variables $u=(hu)/h$ and $v=(hu)/h$ denotes, respectively, the 2-D velocity components. The vector $\mathbf{S}$ contains the source terms; it can be further partitioned into $\mathbf{S}=\mathbf{S_b}+\mathbf{S_f}$, where $\mathbf{S_b}=[0,-g\eta\ \partial_x z,-g\eta\ \partial_y z]^{\mathrm{T}}$ is the topography source term vector and the friction source term vector $\mathbf{S_f}=\left[0,S_{fx},S_{fy}\right]^{\mathrm{T}}$ in which $S_{fx}=-C_f u\sqrt{u^2+v^2}$ and $S_{fy}=-C_f v\sqrt{u^2+v^2}$, with $C_f=gn_M^2/h^{1/3}$ (n_M is the Manning coefficient and g the constant gravitational acceleration).

3. Godunov-Type Flood Model Formulations

Two second-order Godunov-type flood model formulations, solving the SWE, are presented in this section. The first is the nonlocal MUSCL reconstruction approach that extrinsically acts on the finite volume formulation to deliver second-order accuracy, while the second is the more complex DG formulation that intrinsically maintains locality. Here, both formulations are presented for the case of a quadrilateral uniform mesh on which they are proved to achieve second-order convergence [*Wang et al.*, 2011; *Kesserwani and Liang*, 2010].

A 2-D domain $[x_{\min}; x_{\max}]\times[y_{\min}; y_{\max}]$ is subdivided into $M\times N$ cells. A local cell $I_{i,j}=[x_{i-1/2}; x_{i+1/2}]\times[y_{i-1/2}; y_{i+1/2}]$ is centered at point (x_i, y_j), with $x_i=0.5(x_{i-1/2}+x_{i+1/2})$ and $y_j=0.5(y_{j-1/2}+y_{j+1/2})$, and has the dimensions $\Delta x\times\Delta y$, with $\Delta x=x_{i+1/2}-x_{i-1/2}$ and $\Delta y=y_{j+1/2}-y_{j-1/2}$. In what follows, the local approximate flow vector will be denoted by $\mathbf{U_h}$ and, consistently, the local discrete approximation of the topography will be denoted by z_h.

3.1. Finite Volume MUSCL Formulation

The finite volume formulation essentially discretizes the conservative integral form of (1) to produce a local piecewise-constant approximation to the flow variables as well as the topographic profile, i.e., $\mathbf{U_h}(x,y,t)|_{I_{i,j}}=\mathbf{U}_{i,j}=[\eta_{i,j};\ (hu)_{i,j};\ (hv)_{i,j}]^T$ and $z_h(x,y)|_{I_{i,j}}=z_{i,j}$. The discretization yields the following semidiscrete conservative form that is used to evolve the local piecewise-constant data:

$$\frac{d}{dt}\mathbf{U_h}|_{I_{i,j}}=-\frac{1}{\Delta x}\left(\tilde{\mathbf{F}}_{i+1/2,j}-\tilde{\mathbf{F}}_{i-1/2,j}\right)-\frac{1}{\Delta y}\left(\tilde{\mathbf{G}}_{i,j+1/2}-\tilde{\mathbf{G}}_{i,j-1/2}\right)+\mathbf{S_h}|_{I_i} \tag{2}$$

The fluxes, e.g., $\tilde{\mathbf{F}}_{i+1/2,j}=\tilde{\mathbf{F}}^{HLLC}\left(\mathbf{U}^-_{i+1/2,j},\mathbf{U}^+_{i+1/2,j}\right)$ at the interface $(x_{i+1/2,j}, y_{i,j})$ of cell $I_{i,j}$ (shared by the adjacent neighbor cell $I_{i+1,j}$), are obtained by solving the local Riemann problem, here using the HLLC nonlinear flux function combining the limits of the approximate solution at the interface $x_{i+1/2,j}$, which are in essence piecewise constant [*Toro*, 2001]. To obtain a stable second-order accurate scheme, the MUSCL linear interpolation approach is applied to estimate solution limits associated with fictitious piecewise-linear solutions, i.e., reconstructed from the piecewise-constant local evolution flow data [*Van Leer*, 1979]:

$$\mathbf{U}^-_{i+1/2,j}=\mathbf{U}_{i,j}+0.5\nabla_{i,j}(\mathbf{U_h}) \tag{3}$$

$$\mathbf{U}^+_{i+1/2,j}=\mathbf{U}_{i+1,j}-0.5\nabla_{i+1,j}(\mathbf{U_h}) \tag{4}$$

Where,

$$\nabla_{i,j}(\mathbf{U_h})=\varphi\left(\frac{\mathbf{U}_{i,j}-\mathbf{U}_{i-1,j}}{\mathbf{U}_{i+1,j}-\mathbf{U}_{i,j}}\right)(\mathbf{U}_{i,j}-\mathbf{U}_{i-1,j}) \tag{5}$$

In (5), $\varphi(\mathbf{r})=\max\left[0,\min\left(1,\mathbf{r}\right)\right]$ is a limiter function that controls the variation of the slope components to avoid spurious oscillations that would possibly occur around discontinuities [*Toro*, 2001]. Here the *minmod* limiter is adopted in favor of stability despite the question of whether a better choice maybe used [*Sanders and Bradford*, 2006]. The MUSCL approach, followed by the application of the HLLC Riemann solver, gives estimates of the fluxes $\tilde{\mathbf{F}}_{i-1/2,j}$, $\tilde{\mathbf{G}}_{i,j+1/2}$, and $\tilde{\mathbf{G}}_{i,j-1/2}$, at the interfaces $(x_{i-1/2,j}, y_{i,j})$, $(x_{i,j}, y_{i+1/2,j})$ and $(x_{i,j}, y_{i-1/2,j})$, respectively. Finally, time-discretization in equation (2) is achieved using the explicit two-stage Runge-Kutta (RK) time stepping controlled by the Courant-Friedrich-Lewy (CFL) condition with a CFL number equal to 0.5.

3.2. Discontinuous Galerkin Formulation (RKDG2)

For a second-order DG space discretization coupled with a RK time stepping (RKDG2), the sought solution is locally piecewise-linear, or actually planar in 2-D, spanned by three time-evolving coefficients, i.e., $\mathbf{U_h}|_{I_{i,j}}=\left\{\mathbf{U}^0_{i,j},\mathbf{U}^{1x}_{i,j},\mathbf{U}^{1y}_{i,j}\right\}$. That is:

$$\mathbf{U}_{\mathrm{h}}(x,y,t)|_{I_{i,j}}=\mathbf{U}^{0}_{i,j}(t)+\mathbf{U}^{1x}_{i,j}(t)\frac{(x-x_i)}{\Delta x/2}+\mathbf{U}^{1y}_{i,j}(t)\frac{(y-y_j)}{\Delta y/2}\qquad(\forall(x,y)\in I_{i,j})\tag{6}$$

The semidiscrete local transformation to the conservative form, in equation (1), now produces three spatial operators for the (decoupled) update of the local solution coefficients:

$$\frac{d}{dt}\begin{pmatrix}\mathbf{U}^{0}_{i,j}(t) & 0 & 0\\ 0 & \mathbf{U}^{1x}_{i,j}(t) & 0\\ 0 & 0 & \mathbf{U}^{1y}_{i,j}(t)\end{pmatrix}=\begin{pmatrix}\mathbf{L}^{0}_{i,j} & 0 & 0\\ 0 & \mathbf{L}^{1x}_{i,j} & 0\\ 0 & 0 & \mathbf{L}^{1y}_{i,j}\end{pmatrix}\tag{7}$$

Where $\mathbf{L}^{0}_{i,j}$, $\mathbf{L}^{1x}_{i,j}$, and $\mathbf{L}^{1y}_{i,j}$ are the DG2 local discrete spatial projections to the flux and source term vectors in equation (1), which can be worked out to give:

$$\mathbf{L}^{0}_{i,j}=-\frac{1}{\Delta x}\left(\tilde{\mathbf{F}}_{i+1/2,j}-\tilde{\mathbf{F}}_{i-1/2,j}\right)-\frac{1}{\Delta y}\left(\tilde{\mathbf{G}}_{i,j+1/2}-\tilde{\mathbf{G}}_{i,j-1/2}\right)+\mathbf{S}_{\mathbf{h}}|_{I_i}\tag{8}$$

$$\mathbf{L}^{1x}_{i,j}=-\frac{3}{\Delta x}\left\{\tilde{\mathbf{F}}_{i+1/2,j}+\tilde{\mathbf{F}}_{i-1/2,j}-\mathbf{F}|_{I_{i,j}}\left(\mathbf{U}^{0}_{i,j}+\frac{\mathbf{U}^{1x}_{i,j}}{\sqrt{3}}\right)-\mathbf{F}|_{I_{i,j}}\left(\mathbf{U}^{0}_{i,j}-\frac{\mathbf{U}^{1x}_{i,j}}{\sqrt{3}}\right)-\frac{\Delta x\sqrt{3}}{6}\left[\mathbf{S}_{\mathrm{h}}|_{I_{i,j}}\left(\mathbf{U}^{0}_{i,j}+\frac{\mathbf{U}^{1x}_{i,j}}{\sqrt{3}}\right)-\mathbf{S}_{\mathrm{h}}|_{I_{i,j}}\left(\mathbf{U}^{0}_{i,j}-\frac{\mathbf{U}^{1x}_{i,j}}{\sqrt{3}}\right)\right]\right\}\tag{9}$$

$$\mathbf{L}^{1y}_{i,j}=-\frac{3}{\Delta y}\left\{\tilde{\mathbf{G}}_{i,j+1/2}+\tilde{\mathbf{G}}_{i,j-1/2}-\mathbf{G}|_{I_{i,j}}\left(\mathbf{U}^{0}_{i,j}+\frac{\mathbf{U}^{1y}_{i,j}}{\sqrt{3}}\right)-\mathbf{G}|_{I_{i,j}}\left(\mathbf{U}^{0}_{i,j}-\frac{\mathbf{U}^{1y}_{i,j}}{\sqrt{3}}\right)-\frac{\Delta y\sqrt{3}}{6}\left[\mathbf{S}_{\mathrm{h}}|_{I_{i,j}}\left(\mathbf{U}^{0}_{i,j}+\frac{\mathbf{U}^{1y}_{i,j}}{\sqrt{3}}\right)-\mathbf{S}_{\mathrm{h}}|_{I_{i,j}}\left(\mathbf{U}^{0}_{i,j}-\frac{\mathbf{U}^{1y}_{i,j}}{\sqrt{3}}\right)\right]\right\}\tag{10}$$

As with the MUSCL formulation, nonoscillatory solutions around sharp gradients are also ensured, using consistently the *minmod* limiter. However, the slope limiting process must be applied in a localized manner to avoid a number of potential side effects [*Krivodonova et al*., 2004; *Kesserwani and Liang*, 2012a]. After controlling the local slope coefficients, the interfaces fluxes $\tilde{\mathbf{F}}_{i+1/2,j}$, $\tilde{\mathbf{F}}_{i-1/2,j}$, $\tilde{\mathbf{G}}_{i,j+1/2}$, $\tilde{\mathbf{G}}_{i,j-1/2}$ are evaluated in a similar way as for the MUSCL scheme but with a direct evaluation of the limits from the local planar solutions. For example, the solution limits used to estimate the flux $\tilde{\mathbf{F}}_{i+1/2,j}=\tilde{\mathbf{F}}^{HLLC}\left(\mathbf{U}^{-}_{i+1/2,j},\mathbf{U}^{+}_{i+1/2,j}\right)$ at the interface ($x_{i+1/2,j}$, $y_{i,j}$) of cell $I_{i,j}$ are obtained from (6) producing:

$$\mathbf{U}^{-}_{i+1/2,j}=\mathbf{U}_{\mathrm{h}}\left(x_{i+1/2},y_j,t\right)|_{I_{i,j}}=\mathbf{U}^{0}_{i,j}(t)+\mathbf{U}^{1x}_{i,j}(t)\tag{11}$$

$$\mathbf{U}^{+}_{i+1/2,j}=\mathbf{U}_{\mathrm{h}}\left(x_{i+1/2},y_j,t\right)|_{I_{i+1,j}}=\mathbf{U}^{0}_{i+1,j}(t)-\mathbf{U}^{1x}_{i+1,j}(t)\tag{12}$$

The local flux and source term components in (9) and (10) are directly evaluated from the conserved variable information over cell $I_{i,j}$. Finally, the three coefficients of the local solution, i.e., $\mathbf{U}^{0}_{i,j}(t)$, $\mathbf{U}^{1x}_{i,j}(t)$, and $\mathbf{U}^{1y}_{i,j}(t)$, are independently advanced in time using the explicit double-stage RK time discretization, but with a CFL number equal to 0.3 [*Cockburn and Shu*, 2001; *Kesserwani and Liang*, 2012a].

4. Discretization of the Source Terms With Wetting and Drying

Prior to the call to the spatial operator in the MUSCL scheme, i.e., the RHS of equation (2), and to the DG2 operators in (8)–(10), the local numerical solution is reconsidered to ensure accurate and stable discretization of the topography and friction source terms, along with a positivity-preserving water depth. First, in both models, the contribution of the friction source terms is integrated by an implicit splitting discretization to avoid instabilities around those zones with very small water levels, i.e., not directly included in the spatial operators. The technical expressions of the implicit friction term discretization for both the MUSCL and RKDG2 models may be found within *Liang and Marche* [2009] and *Kesserwani and Liang* [2012a, 2012b], respectively. In the MUSCL scheme, the contribution of friction effects is added to the local-averaged discharge variable prior to each time stage and time step. For the RKDG2 scheme, friction effects needed to be further added to the local slope discharge coefficients. Secondly, to deal with topographic discretization and wetting and drying, variants of the hydrostatic reconstruction approach [e.g., *Audusse et al*., 2004; *Mungkasi and Roberts*, 2010] have been improved and tailored to the MUSCL and

RKDG2 frameworks [*Liang*, 2010; *Kesserwani and Liang*, 2010, 2012a], and these are reviewed in the following subsections.

4.1. Discretization Within the MUSCL Formulation

In the MUSCL scheme, the topography is represented as local piecewise constant with discontinuities at interfaces, and the action of the wetting and drying over topography may be summarized in the steps below:

1. *Reconstruct* the flow variable limits at the eastern interface ($x_{i+1/2,j}$, y_j), via equations (3) and (4):

$$\mathbf{U}^-_{i+1/2,j}=[\eta^-_{i+1/2,j},\ \ (hu)^-_{i+1/2,j},\ \ (hv)^-_{i+1/2,j}]^{\mathrm{T}}=\mathbf{U}_{i,j}+0.5\nabla_{i,j}(\mathbf{U})$$

$$\mathbf{U}^+_{i+1/2,j}=[\eta^+_{i+1/2,j},\ \ (hu)^+_{i+1/2,j},\ \ (hv)^+_{i+1/2,j}]^{\mathrm{T}}=\mathbf{U}_{i+1,j}+0.5\nabla_{i+1,j}(\mathbf{U})$$

2. *Reconstruct* the water depth limits at ($x_{i+1/2,j}$, y_j), apply equations (3) and (4) to the $\eta-z$:

$$h^-_{i+1/2,j}=(\eta_{i,j}-z_{i,j})+0.5\nabla_{i,j}(\eta-z)$$

$$h^+_{i+1/2,j}=(\eta_{i+1,j}-z_{i+1,j})-0.5\nabla_{i+1,j}(\eta-z)$$

3. *Evaluate* the associated velocity limits at ($x_{i+1/2,j}$, y_j) when $h^K_{i+1/2,j}>10^{-6}$ (zero them otherwise): $u^K_{i+1/2,j}=(hu)^K_{i+1/2,j}/h^K_{i+1/2,j}$ and $v^K_{i+1/2,j}=(hv)^K_{i+1/2,j}/h^K_{i+1/2,j}$, $(K=+,-)$.

4. Interface topography discretization with wetting and drying:

a. Produce a locally continuous (single) topography value $z^{\pm,*}_{i+1/2,j}$, at $x_{i+1/2,j}$, defined by the maximum: $z^{\pm,*}_{i+1/2,j}=\max\,(z^-_{i+1/2,j},z^+_{i+1/2,j})$, with $z^K_{i+1/2,j}=\eta^K_{i+1/2,j}-h^K_{i+1/2,j}$ $(K=+,-)$.

b. Redefine new depth-positivity-preserving components relative to the new single value of the interface topography: $h^{K,*}_{i+1/2,j}=\max\left(0,\eta^K_{i+1/2,j}-z^{\pm,*}_{i+1/2,j}\right)$ $(K=+,-)$.

c. Revise accordingly the flow variables limits, while preserving the velocities of step (3): $\eta^{K,*}_{i+1/2,j}=h^{K,*}_{i+1/2,j}+z^{\pm,*}_{i+1/2,j}$, $(hu)^{K,*}_{i+1/2,j}=h^{K,*}_{i+1/2,j}\ u^K_{i+1/2,j}$, $(hv)^{K,*}_{i+1/2,j}=h^{K,*}_{i+1/2,j}\ v^K_{i+1/2,j}$ $(K=+,-)$

d. Ensure that the revised depth-positivity-preserving variables does not perturb the well-balanced property at the ($x_{i+1/2,j}$, y_j): first find $\Delta\eta_{i+1/2,j}=\max\left[0,-\left(\eta^K_{i+1/2,j}-z^{\pm,*}_{i+1/2,j}\right)\right]$ and then adjust $\eta^{K,*}_{i+1/2,j}\leftarrow\eta^{K,*}_{i+1/2,j}-\Delta\eta_{i+1/2,j}$ and $z^{\pm,*}_{i+1/2,j}\leftarrow z^{\pm,*}_{i+1/2,j}-\Delta\eta_{i+1/2,j}$.

5. Calculate Riemann flux $\tilde{\mathbf{F}}_{i+1/2,j}$ at ($x_{i+1/2,j}$, y_j) by inputting the new depth-positivity preserving variables, i.e., $\mathbf{U}^{K,*}_{i+1/2,j}$, and modified topography, i.e., $z^{\pm,*}_{i,j+1/2}$, to the HLLC Riemann solver.

6. Repeat steps (1)–(5) to further estimate fluxes $\tilde{\mathbf{F}}_{i-1/2,j}$, $\tilde{\mathbf{G}}_{i,j+1/2}$, $\tilde{\mathbf{G}}_{i,j-1/2}$ at the other three interfaces of cell $I_{i,j}$.

7. Set $\bar{\eta}^x=(\eta^{-,*}_{i+1/2,j}+\eta^{+,*}_{i-1/2,j})/2$, $\bar{\eta}^y=(\eta^{-,*}_{i,j+1/2}+\eta^{+,*}_{i,j-1/2})/2$, $\overline{\partial_x z}=(z^{\pm,*}_{i+1/2,j}-z^{\pm,*}_{i-1/2,j})/\Delta x$, and $\overline{\partial_y z}=(z^{\pm,*}_{i,j+1/2}-z^{\pm,*}_{i,j-1/2})/\Delta y$, and accordingly discretize $\mathbf{S_b}\approx[0,-g\bar{\eta}^x\ \overline{\partial_x z},-g\bar{\eta}^y\ \overline{\partial_y z}]^{\mathrm{T}}$.

4.2. Discretization Within the RKDG2 Formulation

In the RKDG2 method, the above wetting and drying condition is extended to further incorporate a local planar discretization pattern to the topography and the extra slope coefficients defining the local planar solution. Here, the topography is locally discretized as piecewise-planar and is globally continuous, i.e.,

$$z_h(x,y)|_{I_{i,j}}=z^0_{i,j}+z^{1x}_{i,j}\frac{(x-x_i)}{\Delta x/2}++z^{1y}_{i,j}\frac{(y-y_j)}{\Delta y/2}\qquad(\forall(x,y)\in I_{i,j})\tag{13}$$

$$z^0_{i,j}\approx\iint\limits_{I_{i,j}}z(x,y)dxdy\approx\frac{z(x_{i+1/2},y_j)+z(x_{i-1/2},y_j)+z(x_i,y_{j+1/2})+z(x_i,y_{j-1/2})}{4}\tag{14}$$

$$z^{1x}_{i,j}\approx\int\limits_{x_{i-1/2}}^{x_{i+1/2}}\left(\frac{x-x_i}{\Delta x}\right)z(x,y_j)\ dx\approx\frac{z(x_{i+1/2},y_j)-z(x_{i-1/2},y_j)}{2}\tag{15}$$

$$z^{1y}_{i,j}\approx\int\limits_{y_{j-1/2}}^{y_{j+1/2}}\left(\frac{y-y_j}{\Delta y}\right)z(x_i,y)\ dy\approx\frac{z(x_i,y_{j+1/2})-z(x_i,y_{j-1/2})}{2}\tag{16}$$

With this discretization, it is easy to verify that the continuity property holds at the four interfaces of cell $I_{i,j}$, and thus over the whole domain, and that the local topography gradient terms write ∂_x

$z_h(x,y)|_{I_{i,j}}=2z_{i,j}^{1x}/\Delta x$ and $\partial_y z_h(x,y)|_{I_{i,j}}=2z_{i,j}^{1y}/\Delta y$. With this local planar representation of the topography and an RKDG2 numerical solution, the following changes apply to the wetting and drying condition described previously:

1. *Evaluate* the flow variable limits at the eastern interface ($x_{i+1/2,j}$, y_j), via equations (11) and (12): $\mathbf{U}_{i+1/2,j}^{-}=\mathbf{U}_{i,j}^{0}+\mathbf{U}_{i,j}^{1x}$ and $\mathbf{U}_{i+1/2,j}^{+}=\mathbf{U}_{i+1,j}^{0}-\mathbf{U}_{i+1,j}^{1x}$.

2. *Evaluate* the water depth limits at ($x_{i+1/2,j}$, y_j), apply equations (11) and (12) to the $\eta - z$:
$h_{i+1/2,j}^{-}=(\eta_{i,j}^{0}-z_{i,j}^{0})+(\eta_{i,j}^{1x}-z_{i,j}^{1x})$ and $h_{i+1/2,j}^{+}=(\eta_{i+1,j}^{0}-z_{i+1,j}^{0})-(\eta_{i+1,j}^{1x}-z_{i+1,j}^{1x})$.

3. Steps (3)–(6) remain the same as described previously for the MUSCL scheme.

4. Redefine, both locally and temporarily, the local topography and flow variable coefficients according to the well-balanced depth positivity preserving set of revised data:
$\bar{\mathbf{U}}_{i,j}^{0,x}=(\mathbf{U}_{i+1/2,j}^{-,*}+\mathbf{U}_{i-1/2,j}^{+,*})/2$, $\bar{\mathbf{U}}_{i,j}^{1,x}=(\mathbf{U}_{i+1/2,j}^{-,*}-\mathbf{U}_{i-1/2,j}^{+,*})/2$, $\bar{\mathbf{U}}_{i,j}^{0,y}=(\mathbf{U}_{i,j+1/2}^{-,*}+\mathbf{U}_{i,j-1/2}^{+,*})/2$, $\bar{\mathbf{U}}_{i,j}^{1,y}=(\mathbf{U}_{i,j+1/2}^{-,*}-\mathbf{U}_{i,j-1/2}^{+,*})/2$, $\bar{z}_{i,j}^{0x}=(z_{i+1/2,j}^{\pm,*}+z_{i-1/2,j}^{\pm,*})/2$, $\bar{z}_{i,j}^{1x}=(z_{i+1/2,j}^{\pm,*}-z_{i-1/2,j}^{\pm,*})/2$ and $\bar{z}_{i,j}^{0y}=(z_{i,j+1/2}^{\pm,*}+z_{i,j-1/2}^{\pm,*})/2$ and $\bar{z}_{i,j}^{1y}=(z_{i,j+1/2}^{\pm,*}-z_{i,j-1/2}^{\pm,*})/2$.

5. Use *all* coefficients in step (4) to achieve the discretization the local fluxes and source terms within the DG2 spatial operator of equations (8–10).

4.3. Practical Considerations

Despite applying the same wetting and drying condition to the MUSCL and RKDG2 schemes, one notable difference remains particular to each of the models in practice. Although the MUSCL formulation reconstructs a piecewise-linear solution from nonlocal evolution data, such a reconstruction may be impossible around the wet/dry front as the flow data are indefinite in at least one of the neighboring (dry) cell. The use of a global slope limiting process makes this issue even more of a problem at the wet/dry front, making the solution more vulnerable to generating numerical instabilities [*Liang*, 2010]. For stability purposes, therefore, the limiter is switched off in this zone leaving no direct option other than to localize the approximate solution and thereby reduce the local accuracy order to 1. There is a similar requirement for the RKDG2 formulation, but since it is inherently local, it provides an opportunity to maintain a local linear wet/dry front tracking ability given that the limit is entirely switched off around wet/dry zones [*Kesserwani and Liang*, 2012a].

5. Numerical Validation and Comparisons

The conceptual ability of both the MUSCL and RKDG2 numerical formulations in modeling water depth and flow discharge around obstacles and/or through hydraulic jumps has recently been compared for the 1-D case [*Kesserwani*, 2013]. Here selected test cases are used to assess the practical abilities of the local RKDG2 formulation with reference to the MUSCL finite volume formulation addressing questions pertinent to 2-D flood modeling. Two synthetic test cases, with reference data, are first employed to assess the behavior of the two models in the presence of smooth and sharp flow transitions, wave structure interaction, wet/dry front, and nonlinear curved flows, and to quantify issue of runtime saving, mesh convergence and second-order accuracy assessment (when appropriate). Then, the coarse mesh RKDG2 model is qualitatively evaluated for modeling real-scale wave propagation events driven by torrential and fluvial flooding by further contrasting its performance with the MUSCL solver on the same coarse mesh and a finer mesh.

5.1. Dam-Break Wave Interacting With Trapezoidal Obstacle

Ozmen-Cagatay and Kocaman [2011] conducted high-quality water depth experiments for dam-break flow over a dry trapezoidal bottom obstacle. These experiments were supported with 3-D simulations solving the RANS equations. Herein, a selection of these experiments are used to compare the ability of the MUSCL and RKDG2 to reproduce different aspects of shallow flow modeling, including nonlinear dam-break waves, topography-reflected shock, and wetting and drying over an uneven and frictional floodplain. The experiment was carried out in the Civil Engineering Hydraulic Laboratory of the Cukurova University in Turkey using a horizontal channel 8.9 m long, 0.3 m wide, and 0.34 m high. The channel bottom and walls are made of 9 mm thick glass (Manning factor for glass is 0.01 $\mathrm{m}^{1/3}$/s). The dam is located 4.65 m from the channel entrance separating the upstream part of the channel representing the reservoir, which contained an initial water level of $h_0 = 0.25$ m. The initial water depth h_0 is used to normalize the flow depth h/h_0 and longitudinal distance x/h_0.

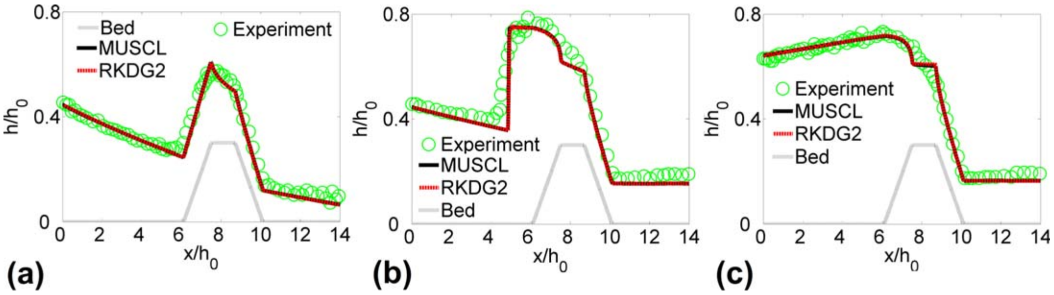

Figure 1. Dam-dreak flow over topogrpahy. MUSCL and RKDG2 simulations on very fine meshes, respectively, 1780 × 60 and 890 × 30, producing similar qualitative results: (a) $T = 11.9$, (b) $T = 23.03$, and (c) $T = 41.84$.

A similar procedure is used for the simulation time, t, to obtain a dimensionless time $T = t\ (g/h_0)^{1/2}$. At $T = 0$, the dam is lifted instantaneously, to generate the dam-break wave for which experimental free-surface profiles were available $T = 11.9$, 23.05, and 41.84. To verify that both MUSCL and RKDG2 formulations are converged, simulations are first produced on carefully chosen fine meshes, i.e., formed by 1780 × 60 and 890 × 30 cells, respectively, until both schemes are observed to reproduce the experimental profiles with similar qualitative accuracy (see Figure 1).

To distinguish between the performances of the two numerical formulations, simulations are now redone on similar mesh configurations, consisting of 40 × 5 (coarse), 80 × 10 (medium), and 160 × 20 (fine) cells, respectively. Figure 2 compares the models' predictions on each of the meshes at three output times.

The RKDG2 model is seen to maintain a very good agreement with the experimental profiles on all the meshes, while the performance of the MUSCL scheme appears to be more reliant on the resolution of the mesh. At $T = 11.9$ and $T = 23.05$, the MUSCL calculations on the coarse and medium meshes differs from both

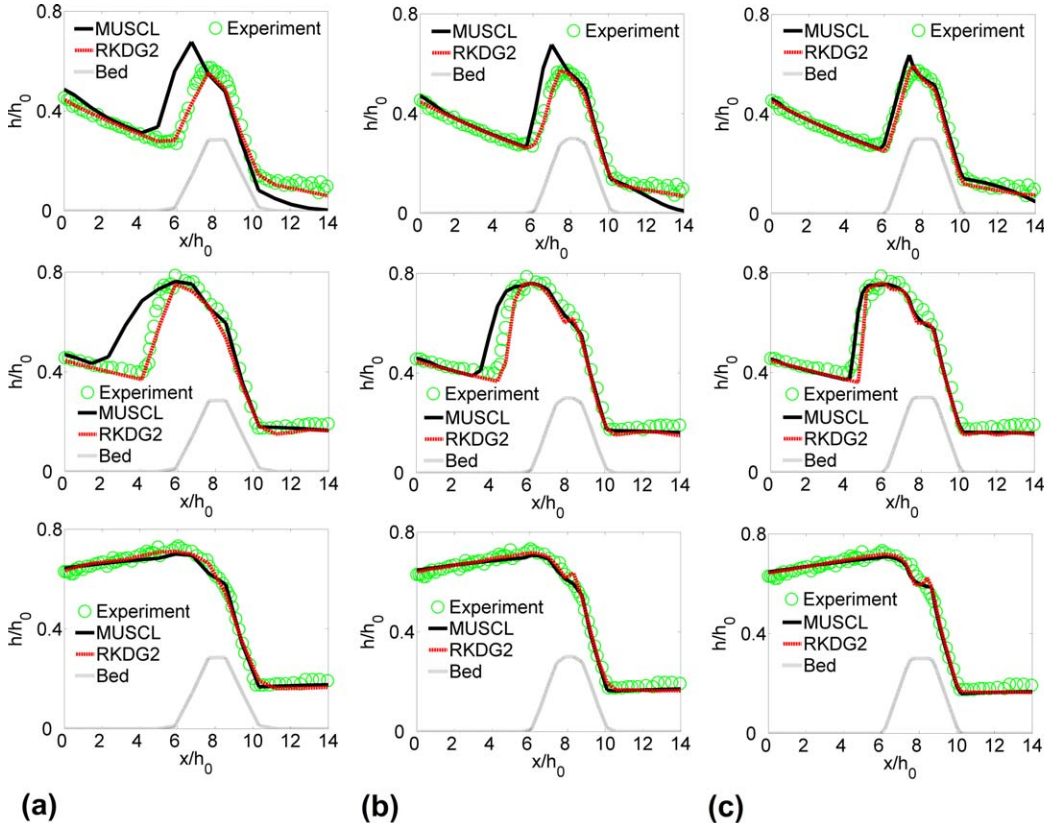

Figure 2. Dam-dreak flow over topography at (top) T = 11.9, (middle) T = 23.05, and (bottom) T = 41.84. Each row shows the MUSCL and RKDG2 free-surface predictions carried out on grids consisting of: (a) 40 × 5 cells, (b) 80 × 10 cells, and (c) 160 × 20 cells.

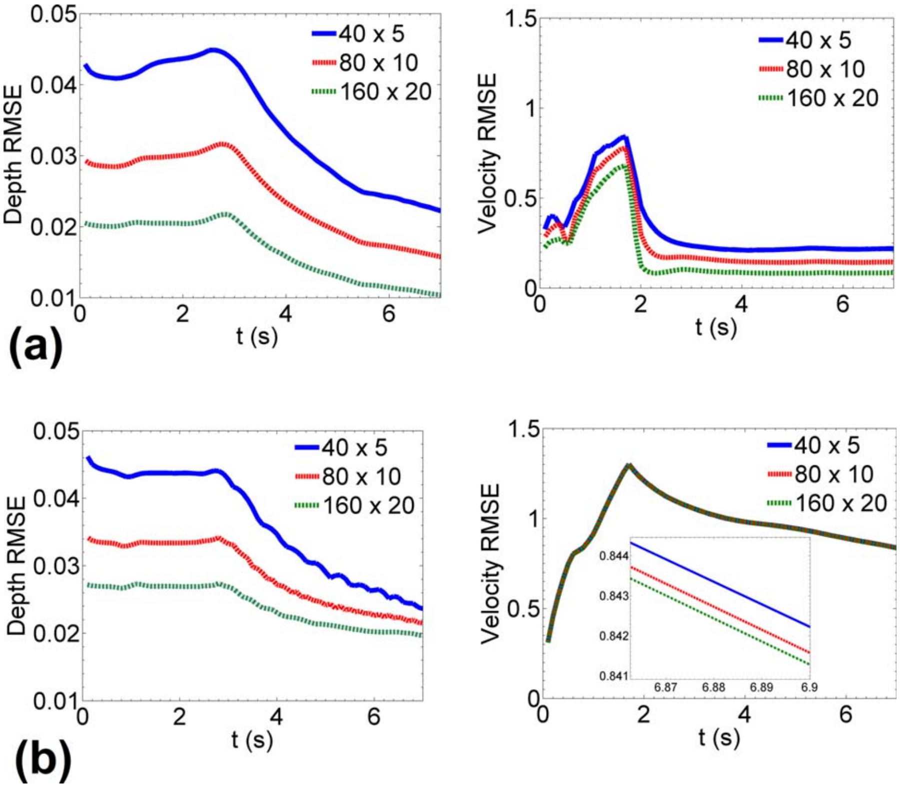

Figure 3. Time evolution of the RMSE relative to the coarse (40 × 5), medium (80 × 10), and fine (160 × 40) meshes using the fine mesh (1780 × 60) MUSCL depth and velocity prediction as reference data: (a) MUSCL formulation and (b) RKDG2 formulation.

the RKDG2 and the experimental profiles. This difference is noted in terms of ability to capture the topography-reflected bore-wave traveling to the upstream and the smooth zone downstream of the obstacle, which occurred after the wetting process. In particular, the MUSCL scheme is seen to slow down the tracking of the wetting process on the coarse mesh, and diffuses the capturing of the bore wave for the coarse and medium meshes. On the fine mesh, however, the MUSCL estimates are found to closely match the experiments and the RKDG2 numerical profiles, especially around the bore wave and downstream of the hump. At $T = 41.84$, when the numerical solution becomes shock free and the domain is fully wet, the coarsening in grid resolution seems to have inconsequential effects on the quality of the MUSCL predictions, which remain very close to the reference data and the RKDG2 predictions for all of the considered meshes.

In addition, the mesh convergence of MUSCL and RKDG2 models is quantitatively analyzed by recording the time histories of root-mean-square-error RMSE (i.e., the L^2-RMSE in equation (20) below) using the MUSCL predictions relative to the highest mesh resolution (i.e., consisting of 1780 × 60 cells) to be the benchmark solution for the RMSE method. Lower-resolution MUSCL and RKDG2 predictions are linearly interpolated to produce a matching resolution. Figure 3 compares the time evolution of the RMSE for both depth and velocity variables, which are produced by the MUSCL and RKDG2 models on the coarse, medium, and fine meshes. In terms of depth predictability, contrast Figure 3a (left) versus Figure 3b (left), the RMSEs relative to the RKDG2 model appear to be more convergent with time evolution, despite the mesh size, as compared to the RMSEs relative to the MUSCL model, which remain stagnant. For the velocity, compare Figure 3a (right) versus Figure 3b (right), the RMSEs delivered by the RKDG2 model are almost the same (differences among them is only noted when considering a zoom in portion) when represented on the same axis scale as those relative to the MUSCL model, which their deviations seem to be much more sensitive to the mesh size. It may be worth stressing that higher magnitude of velocity RSMEs relative to the RKDG2 model is owed to the consideration of the MUSCL data as benchmark—since the two models have different localized behaviors in modeling velocity around topographic flow with shock [*Kesserwani*, 2013].

The implication of these results is that the MUSCL scheme's performance is likely to be valid for coarse mesh simulations when the flow is smooth and the domain is entirely wet, or otherwise the computational

Table 1. Dam-Break Wave Interacting With Trapezoidal Obstacle: Generated Runtime Cost

	MUSCL	RKDG2
40 × 5 (Coarse)	0.47 s	6.48 s
80 × 10 (Medium)	1.44 s	30.58 s
160 × 20 (Fine)	10.58 s	261.23 s

mesh needs to be fine enough to deliver a reliable level of modeling. Unlike the MUSCL scheme, the RKDG2 formulation demonstrates an ability to predict all challenging details of a wave-structure interaction on a very coarse mesh. In terms of runtime cost, the RKDG2 method is undoubtedly more costly to run than the MUSCL scheme on the same mesh setting (see Table 1). However, the RKDG2 model is economical in the sense that it provides very reliable simulations on the coarse mesh, while a simulation of equivalent accuracy with the MUSCL scheme requires a finer mesh and, consequently, takes more time to run.

5.2. Curved Oscillatory Flow in a Parabolic Basin

A similar investigation is done with a more thorough focus on the models' ability to capture a constantly moving wet/dry wavefront over irregular topography and nonlinear smooth flow curvatures. Therefore, a nonlinear oscillatory water flow in a parabolic bowl with a moving shoreline is considered. The domain topography follows a parabolic lake defined over $[-2000;\ 2000]^2$ by:

$$z(x,y)=h_0\left(\frac{x^2+y^2}{a^2}\right) \tag{17}$$

The parameters h_0, r_o, and a are constants ($h_0=20$ m, $a=1500$ m, and $r_0=10$m). Following *Thacker* [1981], analytical solutions are available for a planar or a curved initial free-surface elevation (motionless). The resulting flow will oscillate indefinitely with amplitude of $w=(8gh_0/a^2)^{1/2}$ and a period of $T=(2\pi)/w$ (i.e., $T=9002.2935$ s). For the curved oscillatory flow case, the analytical solution for the free-surface elevation may be written as:

$$\eta(x,y,t)=h_0\left[\frac{\sqrt{1-A^2}}{1-A\cos wt}-\frac{x^2+y^2}{a^2}\left(\frac{1-A^2}{(1-A\cos wt)^2}-1\right)\right] \tag{18}$$

$$A=h_0\left(\frac{a^4-r_0^4}{a^4+r_0^4}\right) \tag{19}$$

Again, the convergence of the MUSCL and RKDG2 formulations are first verified on particular meshes that are fine enough to reproduce the analytical solution with almost similar accuracy, i.e., corresponding to a 2-D grid-scale resolution of 2 and 10 m^2, respectively. The simulations are executed up to one period cycle T, at which the initial condition is expected to be reattained by the numerical models since no friction is acting to damp the momentum of the flow. Figure 4 displays the MUSCL and RKDG2 free-surface predictions along with the analytical solution along the centerline at $y=0$, at four subsequent times, with a step of $T/4$, until one period cycle is achieved. On these particular meshes, both formulations are observed to predict numerical profiles that entirely match the analytical profile, demonstrating thereby their general validity in dealing with nonlinear curved flow where both wetting and drying occur.

To study the response of both formulations to a coarsening of spatial resolution, the solutions were reassessed on a similar mesh with three different resolutions of 40 m^2 (coarse), 20 m^2 (medium), and 10 m^2 (fine), respectively. The free-surface centerline profiles reproduced by the MUSCL and RKDG2 schemes, on the coarse, medium, and fine meshes, at the same output times as before, are illustrated in Figure 5.

For this type of flow, as Figure 5 indicates, the coarseness of the mesh seems to have a major impact on the reliability of the MUSCL predictions of the moving wet/dry shoreline and the flow curvature. On the coarse and medium meshes, the MUSCL scheme again slows down to the trail of the wet/dry front at a wetting stage (e.g., at $T/4$ and $T/2$), whereas it appears to accelerate its pace at the drying stage (e.g., by $3T/4$ and T). However, on the fine mesh, the MUSCL model provided a much improved capture to the dynamic wet/dry front. As to the capture of nonlinear flow curvatures, the MUSCL scheme's calculations appear to be appropriate for all the meshes at $T/4$, slightly deviate from the analytical solution at $T/2$ and $3T/4$ on the coarse and medium meshes, and clearly underperform at time T despite showing a tendency to improve the modeling of flow curvature with refinement of the mesh. In contrast, the RKDG2 model produces excellent predictions of both the moving shoreline and the flow curvature on the coarsest mesh selected.

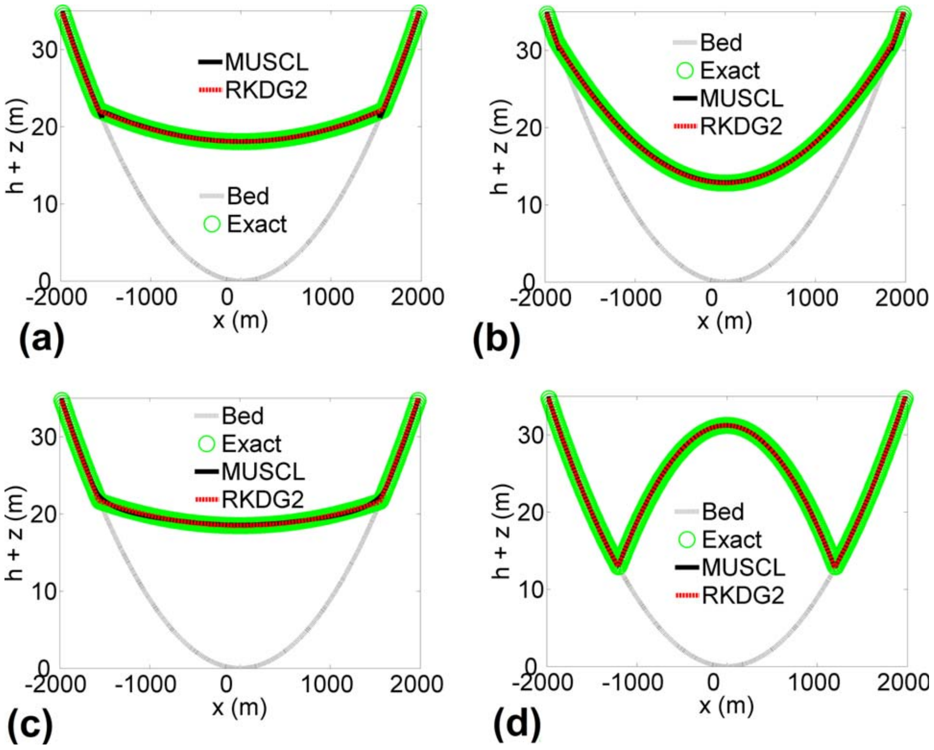

Figure 4. Nonlinear oscillatory flow in a parabolic basin. MUSCL and RKDG2 free-surface predictions are shown for fine meshes, i.e., resolution of 2 and 10 m^2, respectively. This reproduces closely the analytical solution at: (a) *T*/4, (b) *T*/2, (c) 3*T*/4, and (d) *T*.

To allow a quantifiable validation, errors and associated numerical accuracy orders are calculated considering model runs on meshes with four different resolutions. In so doing, the RMSE metric is reevaluated as done in the previous test, i.e., based on the L^2-norm, and considering also the L^1-norm; namely the following expression are used in the RMSE calculations:

$$L^2\text{-}RMSE=\sqrt{\frac{\sum_{i=1}^{M}\left(\mathbf{U}_i^{Exact}-\mathbf{U}_i^{Num.}\right)^2}{M}}\ \text{and}\ L^1\text{-}RMSE=\sqrt{\frac{\sum_{i=1}^{M}\left|\mathbf{U}_i^{Exact}-\mathbf{U}_i^{Num.}\right|}{M}} \qquad (20)$$

Tables 2 and 3 lists the L^2-RMSE and associated orders generated by both MUSCL and RKDG2 estimation to the conservative variables (i.e., η and *hu*) at output times *T*/2 and *T*, respectively; whereas the L^1-RMSE and associated orders for these same calculations, are displayed in Tables 4 and 5.

In terms of discharge predictions, analyzing the L^2-RMSE data in Tables 2 and 3, the RKDG2 model reveals improved second-order convergence rates (i.e., in the range of 2.0–2.3) over the MUSCL scheme (i.e., in the range of 1.3–2.1); especially at time *T* when the MUSCL scheme comparatively deteriorates accuracy down to 1.3 (contrast Table 2 versus Table 3). Almost the same is observed for the L^1-RMSE data, in Tables 4 and 5, albeit at lower overall convergence rates (ranging between 1.4 and 1.8 for the RKDG2, and 0.9 and 1.7 for the MUSCL); at time *T* numerical accuracy of the L^1-RMSE is much more consistent and close to 2.0 for the RKDG2 scheme as compared with those of the MUSCL scheme, which are noted closer to 1.0. Irrespective of the RSME metric used, the discharge errors magnitude for RKDG2 results is always detected to be, at least, one order less than with the MUSCL results.

In terms of free-surface predictions, the numerical orders of accuracy delivered by both MUSCL and RKDG2 models are quite consistent for both L^2-RMSE and L^1-RMSE data (in the range of 1.6–2.1). Moreover, both RMSEs are identified to have close order-of-magnitude despite the slightly improved RSMEs produced by RKDG2 model. Arguably, the more consistent performance observed for the free-surface prediction may be attributed to the fact that: (i) the MUSCL runs are performed on relatively fine meshes to test accuracy; (ii) the variation of the free-surface variable smooth, thus is less exposed to slope zeroing by the *minmod*

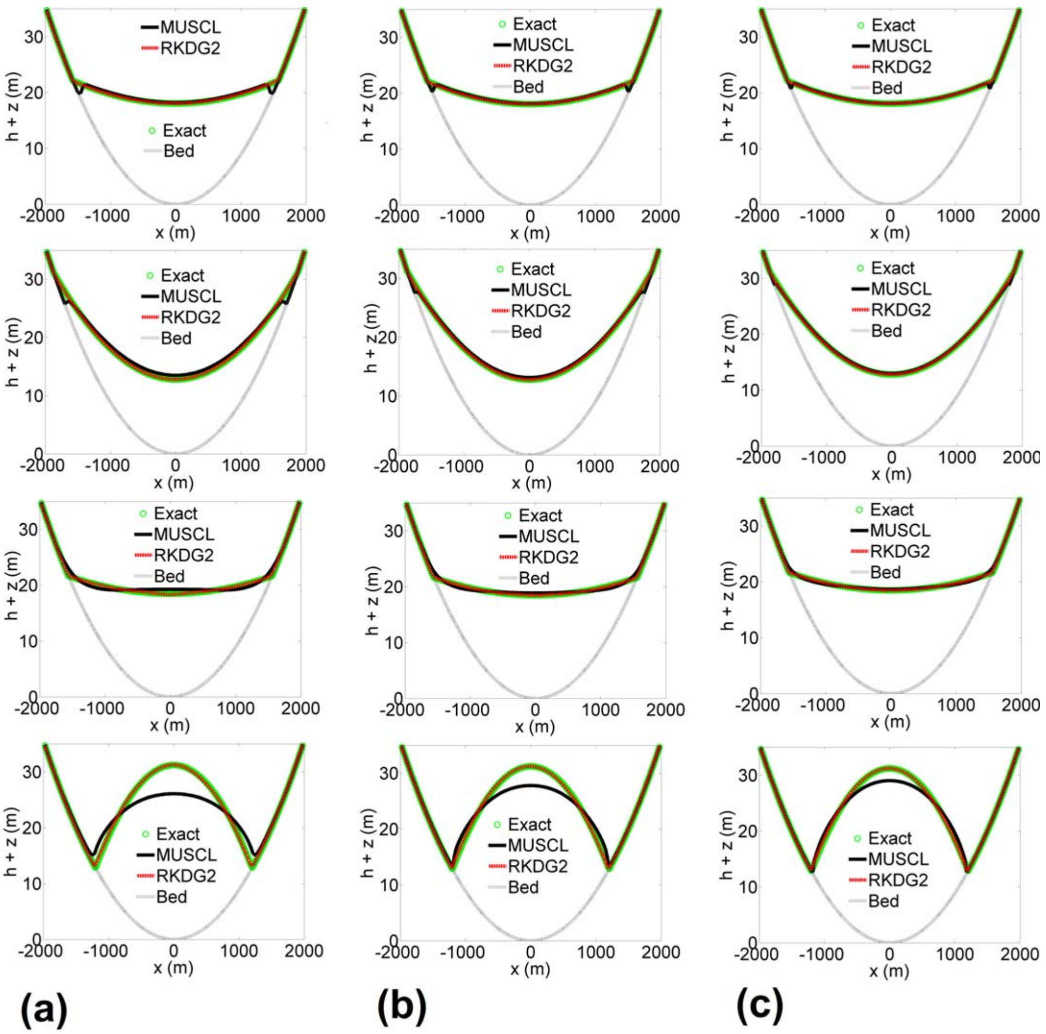

Figure 5. Curved oscillatory flow in a parabolic basin plotted every quarter of a period time and commencing from *T/4* in the top row. Each row shows the MUSCL and RKDG2 predictions carried out on different meshes from coarse to fine with a resolution of: (a) 40 m^2, (b) 20 m^2, and (c) 10 m^2.

limiter; (iii) the topography and friction source terms are indirectly involved in the resolution of the continuity equation as opposed to the case of the momentum equation; (vi) the accuracy drop (to 1.0) accommodating the wet/dry front calculation is local and temporal and will be overwritten by second-order prediction once this portion of the domain becomes wet again.

Overall, the RKDG2 model shows tendency to more consistently conserve the quality of numerical errors and orders produced despite the RSME metric used, the mesh size and the transient nature of the flow. In particular, these results stand out the ability of the RKDG2 model to produces more accurate and sustainable velocity predictions than the MUSCL model irrespective of wet/dry front transients.

Figure 6 displays the numerical velocity calculated by the MUSCL and RKDG2 models consistent with the mesh resolutions and output times available in the tables. At *T*/2, the MUSCL velocity predictions are observed to increasingly diffuse with resolution coarsening; however, this observation does not occur with the RKDG2 velocity calculations, which remain very close to the analytical solution even for the coarsest mesh setting (Figure 6a (left) versus Figure 6a (right)). At the wet/dry shoreline, both models are seen to produce spurious velocity peaks, which are noted to be more localized and reduced for the RKDG2 predictions. At time *T*, the MUSCL model is identified to further present a poor capture to the vanishing velocity on the meshes with a grid resolution coarser than 10 m^2—it could only predict the analytical velocity for the finest resolution considered (Figure 6b, left). This poor behavior is no detected to occur within the

Table 2. Curved Oscillatory Flow in a Parabolic Basin: L2-RMSE and Orders at Time T/2

	MUSCL				RKDG2			
	hu (m^2/s)		η (m)		*hu* (m^2/s)		η (m)	
$M \times N$	L^2-error	L^2-order	L^2-error	L^2-order	L^2-error	L^2-order	L^2-error	L^2-order
100 × 100	1.5E-1		4.3E-2		4.8E-3		2.6E-2	
200 × 200	4.5E-2	1.8	1.4E-2	1.5	1.2E-3	2.0	8.6E-3	1.6
400 × 400	1.2E-2	1.9	4.3E-3	1.7	3.0E-4	2.0	2.6E-3	1.7
800 × 800	2.6E-3	2.1	1.0E-3	2.0	6.8E-5	2.1	6.1E-4	2.1

RKDG2 velocity calculations, which are rather consistent with the analytical solution for all meshes (Figure 6a, right). We argued that such a decline in the MUSCL approach is likely to be caused by the nonlocality of its calculation stencil at wet/dry front where both the friction and/or the wetting and drying discretizations may become conflicting [*Hou et al*., 2013]. Here, first-order local calculation stencil is *temporarily* restored at the wet/dry front to alleviate this conflict, which is also expected to contribute to the observed deterioration in the quality of MUSCL's velocity predictions [*Kesserwani*, 2013].

Table 6 lists runtime costs for this test for mesh setting of resolution ranging between 2.5 and 40 m^2. As expected, the RKDG2 scheme is much more costly than the MUSCL scheme on a similar mesh configuration; this cost is noted to intensify with increasing level of grid resolution. It is worth noting that the extra RKDG2 expense in runtime is associated with the local planar wet/dry front tracking ability of the RKDG2 model. This is expected to increase with smaller time steps and more complex interactions when topography is resolved at higher resolution. Nevertheless, in this test, the RKDG2 model on the coarsest mesh resolution (i.e., of 40 m^2) remains less costly than the MUSCL model on finer mesh resolutions (i.e., of smaller than 10 m^2) and, in this respect, can be classified as economically efficient. Taken as whole, the RKDG2 model appears to be an accurate and reliable alternative for coarse mesh simulation of nonlinear shallow water flow involving cyclic wetting and drying processes.

5.3. Dam-Break Wave Propagating Into the Toce River Valley

The RKDG2 and the MUSCL models are applied to simulate the aftermath of a dam-break wave occurring in and interacting with an initially dry and rough natural terrain obtained from the 1:100 scaled 5 km Toce River reach in the Northern Alps, Italy (see Figure 7). Experimental data on the propagation characteristics of the surge wave following the dam break are available describing the celerity and amplitude of traveling wave at 10 gauging stations, marked in Figure 6.

The terrain data were scaled down to a resolution of 0.05 m^2 covering the 2-D domain, which is 55 m long and 13 m wide and includes an empty reservoir located roughly at the middle at the domain (see Figure 7). The wave propagating into the floodplain is assumed to be driven by a discharge hydrograph from an upstream inflow tank. The inflow boundary condition data set for the flow hydrograph may be obtained from the data sets provided by the CADAM project [*Soares Frazao and Testa*, 1999]. A free outlet boundary is specified at the downstream end and the Manning coefficient for the test is o.o162 s/$m^{1/3}$ [*Soares Frazao and Testa*, 1999]. The RKDG2 and MUSCL models are run on a mesh formed by 40 × 40 cells (coarse), which correspond to a 2-D grid resolution close to 1 m × 0.3 m. Time series obtained from the output of the two models are displayed in Figure 8 along with experimental free-surface elevations. Modeling was undertaken

Table 3. Curved Oscillatory Flow in a Parabolic Basin: L^2-RMSE and Orders at Time *T*

	MUSCL				RKDG2			
	hu (m^2/s)		η (m)		*hu* (m^2/s)		η (m)	
$M \times N$	L^2-error	L^2-order	L^2-error	L^2-order	L^2-error	L^2-order	L^2-error	L^2-order
100 × 100	7.6E-1		1.0E-1		7.1E-2		4.2E-2	
200 × 200	3.0E-1	1.3	3.0E-2	1.6	1.4E-2	2.2	1.4E-2	1.6
400 × 400	1.0E-1	1.5	1.0E-2	1.7	3.2E-3	2.1	4.2E-3	1.7
800 × 800	2.6E-2	2.0	2.0E-3	2.2	6.5E-4	2.3	1.0E-3	2.1

Table 4. Curved Oscillatory Flow in a Parabolic Basin: L^1-RMSE and Orders at Time $T/2$

	MUSCL				RKDG2			
	hu (m^2/s)		η (m)		hu (m^2/s)		η (m)	
$M \times N$	L^1-error	L^1-order	L^1-error	L^1-order	L^1-error	L^1-order	L^1-error	L^1-order
100 × 100	1.1E-0		2.7E-1		3.5E-2		2.1E-1	
200 × 200	4.5E-1	1.3	1.2E-1	1.1	1.3E-2	1.4	9.9E-2	1.0
400 × 400	1.7E-1	1.4	5.2E-2	1.2	5.1E-3	1.4	4.2E-2	1.2
800 × 800	5.0E-2	1.7	1.6E-2	1.6	1.5E-3	1.7	1.4E-2	1.6

with the MUSCL scheme on a fine mesh of 400 × 100 cells. It is pointed out that setting and running the RKDG2 model on the fine mesh is outside the scope of this exercise (and the following real-scale test).

As Figure 8 shows, the RKDG2 predictions on the coarse mesh are in better overall agreement with the experimental data at all the gauging points apart from point G5 where the RKDG2 model relatively underpredicted the experiments. This discrepancy is likely to be attributed to the different strategy adopted by the RKDG2 model in the spectral representation of the topography data. Comparing with the MUSCL predictions, the RKDG2 model outperforms on the coarse mesh where it provides more accurate and consistent prediction of the celerity and magnitude of a torrential flood wave. This test, therefore, suggests that the RKDG2 formulation demands much less grid-resolution details to forecast torrential flooding with equal accuracy to the high-resolution finite volume MUSCL counterpart. Further information on this can be seen in Figure 9, which contrasts the water depth maps predicted by the MUSCL and RKDG2 models on the coarse mesh, at 180 s, versus the fine mesh MUSCL predictions. With reference to the water depth map produced by the fine mesh MUSCL scheme, the coarse mesh RKDG2 is seen to provide a much more consistent depth map on the coarse mesh than the MUSCL scheme, which appears to comparatively magnify the predictions. On the coarse mesh, the 180 s RKDG2 simulations required around 131 s of runtime, while the MUSCL scheme cost 16.09 s (i.e., roughly 8 times less). However, the runtime cost consumed by the MUSCL scheme on the fine mesh is 1123.26 s, which is roughly about 8.5 times more than the RKDG2 scheme on the coarse mesh, for this test. These findings support the use of the RKDG2 model as a justifiable and rational alternative for torrential flood modeling over natural terrain, using low-resolution meshes to obtain simultaneous benefits in both accuracy of output and runtime efficiency.

5.4. Fluvial Urban Flooding Scenario

The RKDG2 and MUSCL models are finally applied to assess a flood inundation scenario occurring at Thamesmead, located on the south bank of the River Thames in London. The dimensions of the flooding domain is 9 × 4 km^2 and its landscape features—available for a 10 m^2 grid resolution DTM data set—is shown in Figure 10a. A 150 m wide breach of the river Thames' bank, centered at (545.855; 181.040), is assumed to create and drive the water inundation into the Thamesmead area; the hydrograph describing the inflow at the breach is illustrated in Figure 10b.

A uniform Manning roughness coefficient of 0.035 m$^{-1/3}$/s is used and simulations are designed to forecast the behavior of the water inundation up to 10 h after the dam breach (i.e., 36,000 s). Since no reference data are available for this test, a MUSCL scheme simulation is first performed on a mesh of 900 × 400 cells, which matches the resolution of the terrain data set, and will be treated as a reference prediction. Subsequently, the MUSCL and RKDG2 schemes are executed on a coarse mesh consisting of 225 × 100 cells, i.e.,

Table 5. Curved Oscillatory Flow in a Parabolic Basin: L^1-RMSE and Orders at Time T

	MUSCL				RKDG2			
	hu (m^2/s)		η (m)		hu (m^2/s)		η (m)	
$M \times N$	L^1-error	L^1-order	L^1-error	L^1-order	L^1-error	L^1-order	L^1-error	L^1-order
100 × 100	5.1E-0		8.5E-1		4.8E-1		3.8E-1	
200 × 200	2.7E-0	0.9	4.0E-1	1.1	1.3E-1	1.8	1.8E-1	1.1
400 × 400	1.3E-0	1.0	1.7E-1	1.2	4.2E-2	1.7	7.7E-2	1.2
800 × 800	4.3E-1	1.5	5.1E-2	1.7	1.2E-2	1.8	2.5E-2	1.6

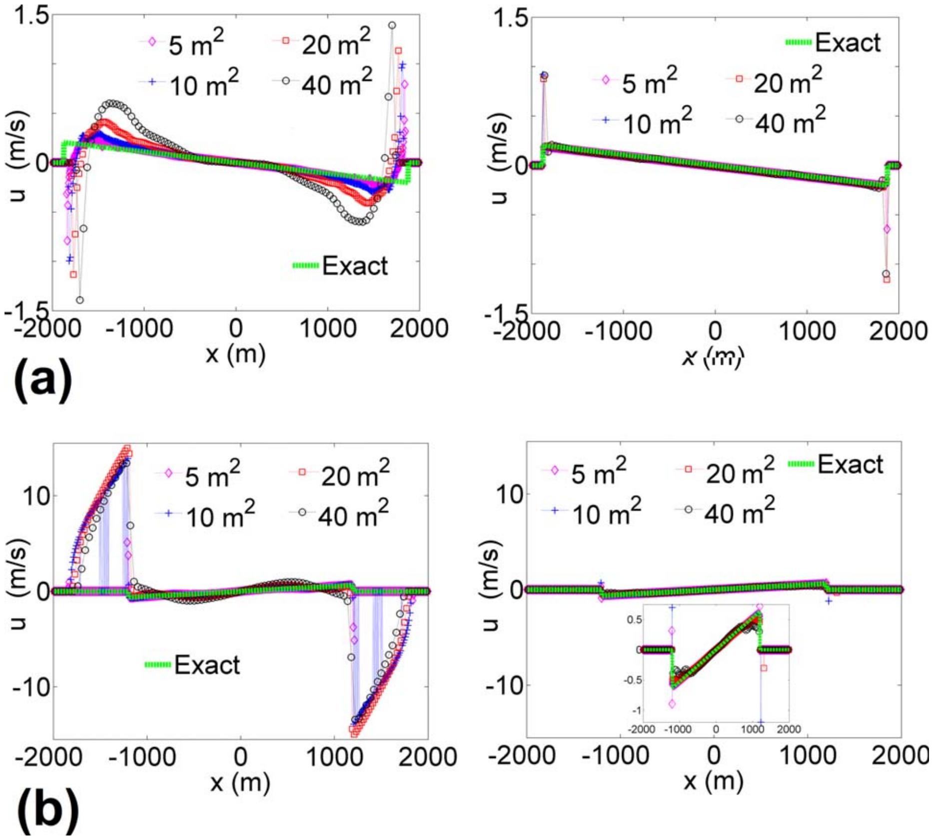

Figure 6. velocity profiles achieved by the (left) MUSCL and (right) RKDG2 models on the four meshes listed in Tables 2 and 3 (i.e., of resolution 40, 20, 10, and 5 m^2, respectively): (a) after half period *T*/2 and (b) after one period *T*.

a 2-D grid-scale resolution of 40 m^2. Figure 11 displays the flood maps produced by the MUSCL and RKDG2 coarse mesh models at $t = 10$ h as well as the reference prediction.

The visual prediction of the flow patterns delivered by the coarse mesh RKDG2 model is seen to match very well the reference predictions; in contrast the coarse mesh MUSCL simulation appears to comparatively overlook a great deal of modeling details and to drastically exaggerate the extent of the flooding event at the eastern part of the domain. In contrast, the coarse mesh RKDG2 prediction appears to respond to forcing from the topographic features in a more realistic manner, looks more interactive with the topographic features and has led to more detailed and wider forecast to the flood propagation. The previous tests in this paper indicate that the more detailed RKDG2 model forecast of the flooding event is likely to be associated with improved, local planar resolution to the topographic domain as well as more accurate wet/dry front tracking. In this example, the effect of enhancing these aspects of the numerical method has a clear impact on the quality of the output, even over a long duration simulation. Figure 12 displays histories of the water depth recorded by the different models at four gauging points, G1, nearest to the breach, G10, farthest from the breach toward the south-east, G4 and G7 located closest to the line (G1, G10). At G1, both coarse mesh models seems to accelerate arrival time relative to the fine mesh predictions; despite this the RKDG2 model shows a better ability to conform to the reference prediction. Similar patterns are observed at G7 where the RKDG2 depth behavior follows closely the reference calculation despite presenting a delay in the prediction of the arrival time. At G4 and G10, the coarse mesh RKDG2 model predicts better the arrival times, generically correlates well with the MUSCL calculations on both fine and coarse meshes but ultimately predict slightly higher water levels.

Table 6. Curved Oscillatory Flow in a Parabolic Basin: Generated Runtime Costs

Runtime Cost (s)	MUSCL	RKDG2
40 m^2 resolution	2.34 s	155.69 s
20 m^2 resolution	19.44 s	1059.53 s
10 m^2 resolution	162.98 s	9518.70 s
5 m^2 resolution	2867.98 s	36423.25 s
2.5 m^2 resolution	66255.23 s	231948.29 s

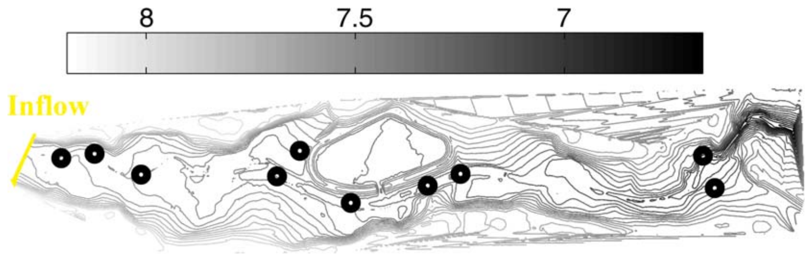

Figure 7. Toce river valley's domain on a grid with a resolution of 0.05 m^2 and including the location of 10 gauging points at which experimental time histories of the free-surface levels are available.

The RKDG2 coarse mesh simulation for this case lasted around 3.5 h, making it even more expensive than the MUSCL scheme on the fine mesh, which took about 2.1 h to run. In contrast, the coarse mesh MUSCL scheme did the job in a matter of minutes (i.e., 16 min). In this test, the overload in runtime associated with the RKDG2 model is to be expected since it wets a larger portion including those extra zones with very low water levels. In fact, the RKDG2 model requires, at the very least, three times more operations—for each space and time discretization and the friction integration—than the MUSCL scheme to achieve a local calculation. In addition, its time step, despite being theoretically less restrictive than for the MUSCL, will be reduced to yield a converged solution to the wetting and drying problem because of the use of the local planar resolution approach. Nevertheless, the RKDG2 provides a much more detailed picture of the flooding event on relatively coarse resolution terrain data and, despite the uncertainty associated with the use of 10 m^2 to be the finest resolution (i.e., not to capture buildings and small surface features in urban flooding).

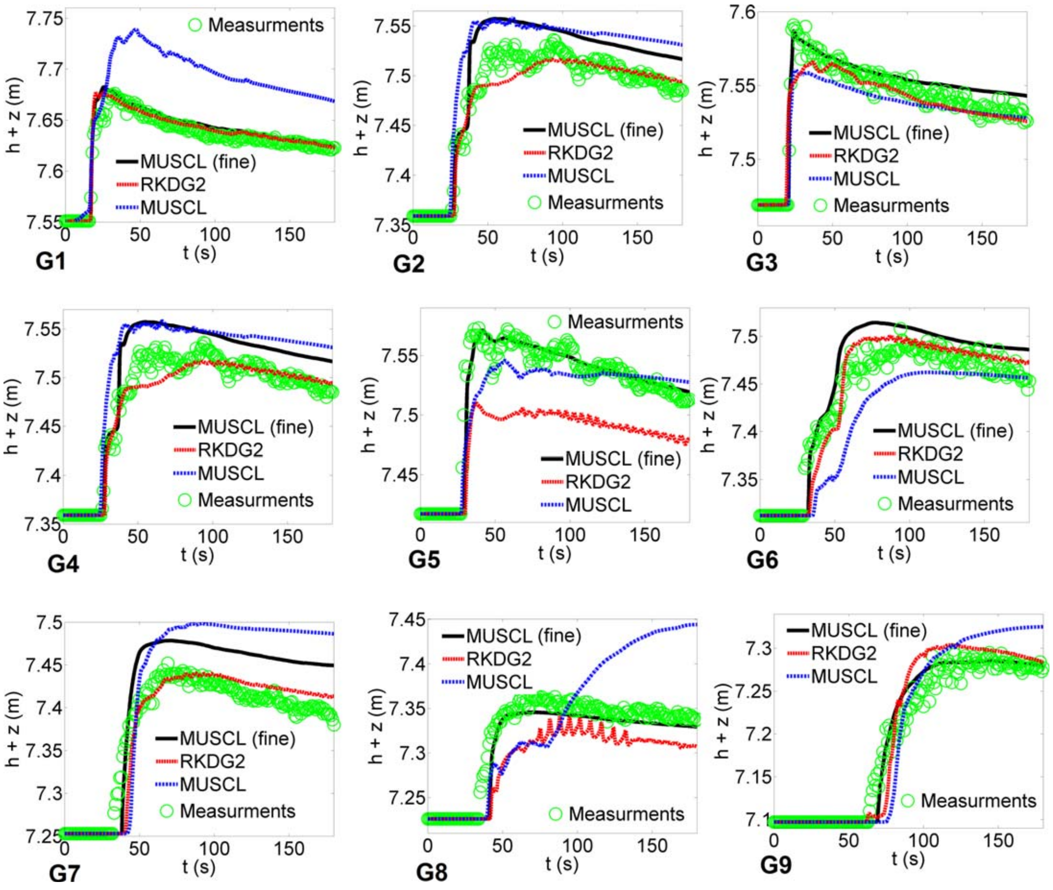

Figure 8. MUSCL and RKDG2 prediction of time histories on a coarse mesh formed by 40 × 40 cells, compared with the experiment and the MUSCL simulation on fine mesh of 400 × 100 cells.

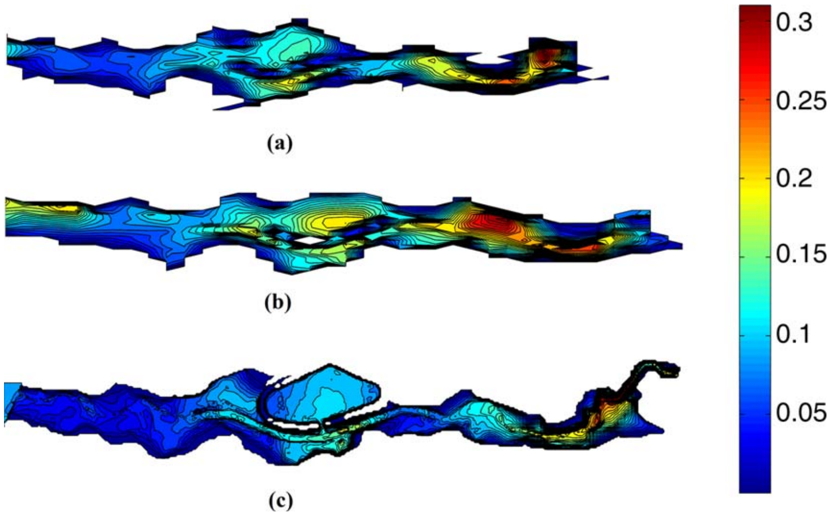

Figure 9. Toce river valley; water depth maps prediction at $t = 180$s: (a) RKDG2 scheme on the mesh 40 × 40, (b) MUSCL scheme on the mesh 40 × 40, and (c) MUSCL scheme on the mesh 400 × 100.

Although future improvement and assessment of the RKDG2 flood model based on more accurate high-resolution terrain data may further be required, this initial contribution offers profound insight into the promise of the RKDG2 formulation as a useful alternative to deal with the forecast of flooding at zones with limited landscape information.

6. Summary and Conclusions

Computational flood models, based on the local finite volume Godunov (first-order) formulation, have received a great deal of practical improvement, becoming a key component of the hydraulic software industry. Higher-order finite volume variants have been proposed in research studies, but they dictate wider (nonlocal) calculation stencils, which is not in the spirit of Godunov's conceptual foundation. Therefore, the most usable finite volume Godunov-type flood models are often first-order accurate and may be second-order accurate when coupled (extrinsically) with MUSCL linear interpolation scheme. Either way, the mathematical/numerical formulation is quite similar and can be considered the most complex techniques currently being used in water resource modeling, particularly flooding. The question of whether an even more complex flood model formulation is needed, and is of utility for further improving flood modeling, is therefore of both theoretical and practical interest.

This work has tackled this question, considering the case of the local Discontinuous Galerkin (DG) formulation, which constitutes a more complex and rigorous extension to the local Godunov conceptual

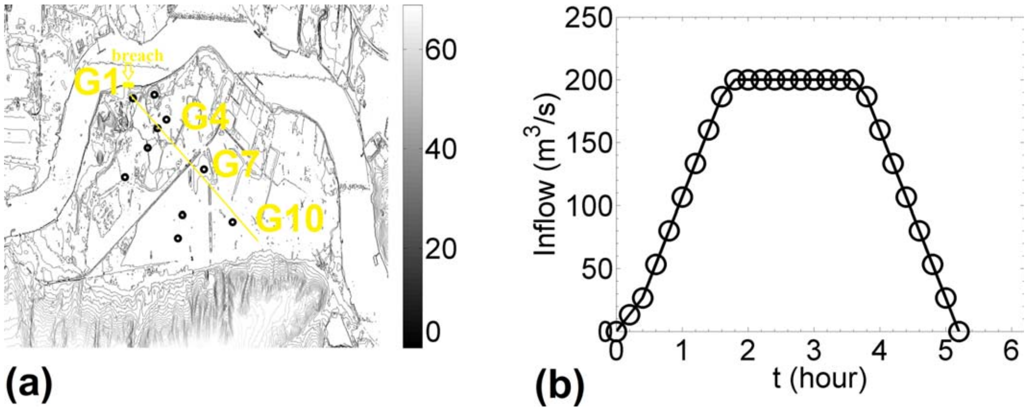

Figure 10. Fluvial flooding in Thamesmead areas: (a) contour line representing the topographic features with a resolution of 10 m^2 and (b) inflow hydrograph at the breach driving the flood event.

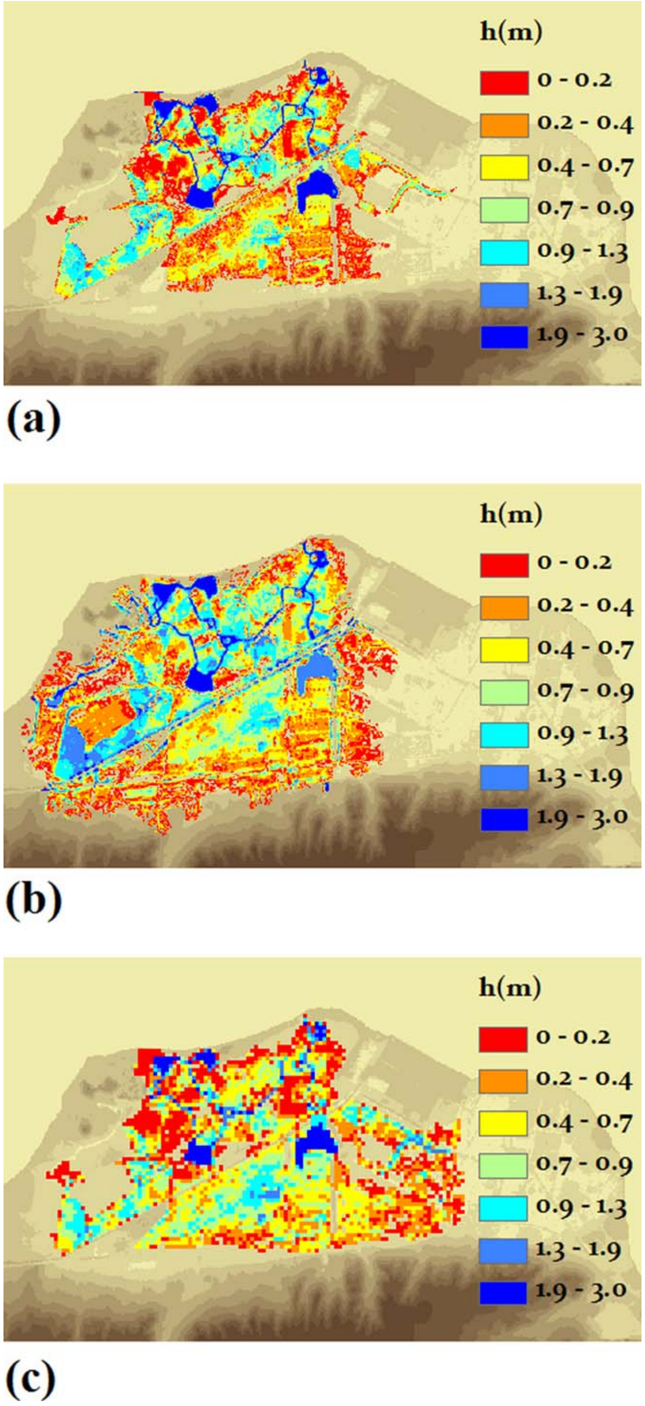

Figure 11. Thamesmead flood inundation. Free surface maps predictions at $t = 10$ h: (a) MUSCL fine (900 × 400 cells), (b) RKDG2 coarse (225 × 100 cells), and (c) MUSCL coarse (225 × 100 cells).

foundation. It has investigated the performance of a second-order local DG flood model formulation (RKDG2) contrasting with the traditional finite volume MUSCL counterpart. Both formulations made use of the same characteristics for time discretization, slope limiting, wetting and drying fronts, among others. The finite volume formulation inherently uses piecewise-constant evolution data and one local space-time operator to achieve a local calculation for the flood flow variables. In contrast, the RKDG2 formulation locally stores 3 times the amount of evolution data to provide an inherently local planar solution with its own local space-time operator. The topography was discretized in a manner consistent with the local discretization pattern of each model. To ensure stability around high-gradient parts of the solution, where wetting and drying may occur, the slope limiter was locally switched off around wet/dry zones in both formulations. With this, the MUSCL finite volume formulation's wet/dry front tracking is localized as piecewise-constant, whereas the RKDG2 solution could be set to provide local planar resolution to wetting and drying. The capabilities of the two formulations were explored for diagnostic and real-scale tests incorporating all challenging features relevant to flood modeling.

The preliminary (diagnostic) testing confirms that both MUSCL and RKDG2 Godunov-type formulations are second-order accurate and valid when the mesh is fine enough, i.e., both showing identical behavior in the capture of the nonlinear and realistic features of shallow water wave modeling. With coarsening of the mesh, results from the (MUSCL) finite volume formulation deteriorate relative to the RKDG2 formulation, which remains comparatively unaffected. In particular, there is comparatively a drastic deterioration in terms of delay in the wetting process, acceleration in both the drying process and the capture of hydraulic jumps, diffusive prediction in regions of high flow curvature and calculation of the vanishing the velocity at moving wet/dry shoreline. However, the behavior of the coarse mesh MUSCL solution remains comparable with the RKDG2

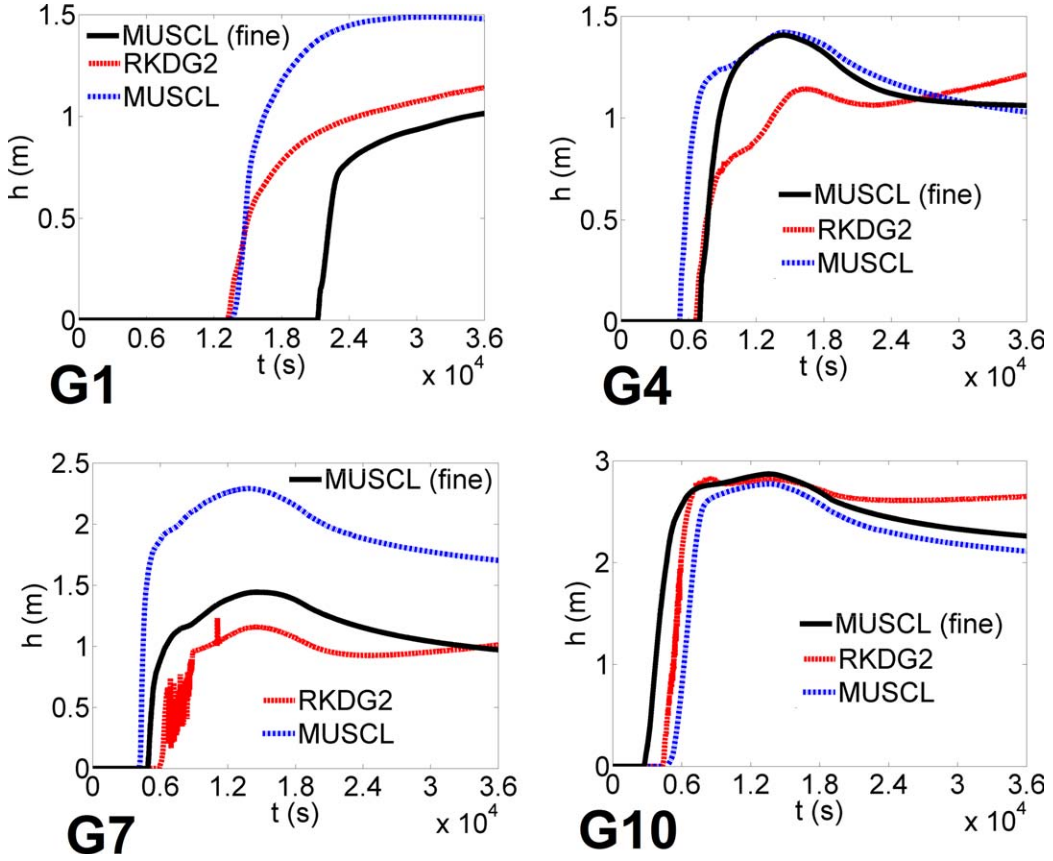

Figure 12. depth evolution predicted by the MUSCL and RKDG2 models on the coarse mesh compared to the MUSCL reference prediction on the fine mesh.

model's outputs when the flow transitions are gradual and the domain is entirely wet. On a similar mesh resolution, the RKDG2 formulation provides finer modeling of shock propagations/reflections and of the interaction with topographic structures when wetting and drying has occurred. In terms of runtime cost, the RKDG2 formulation is more expensive; indeed the extra costs are likely to be associated with the further complexity of its spatial operators, the need to update all the local solution's coefficients at a time, the more restrictive CFL time step condition that would further reduce owing to the more accurate planar tracking of wet/dry fronts, and the more complex friction term discretization. Considering these, the 2-D-RKDG2 formulation is expected to be at least about 10 times more costly to run than the 2-D-MUSCL formulation. On the other hand, the RKDG2 formulation delivers an improved convergence on coarser meshes, without notable degradation in the quality of the modeling output. In this respect, it is economical as comparative results to using the MUSCL formulation, which requires much finer meshes. Further testing was based on two realistic flood propagation scenarios featuring torrential flow and a more fluvial flow. In both cases, the RKDG2 formulation predominantly outperformed the MUSCL formulation in predicting a more realistic picture of the flooding events on meshes with reduced resolution details. For a quite short simulation, i.e., 1.5 h, involving torrential flood wave propagation, the coarse mesh RKDG2 formulation is found to be beneficial in terms of both accuracy and economy over the finite volume equivalent on the fine mesh. On the other hand, for a longer time simulation, i.e., 10 h, for a much slower (fluvial) flood wave propagation, the coarse mesh RKDG2 formulation gave comparable forecasts as that rendered by the fine mesh finite volume formulation; but it required more time to run. This is a consequence of its more accurate planar representation of topography and wetting and drying, which leads to an overall wider flooding extent. These findings mean that the more complex RKDG2 formulation is likely to be promising in practice, most particularly for risk assessments associated with dam-break flood problems and for improving flood flow predictions at zones with limited, or coarse, terrain data. Whether it would meet, or improve, the runtime efficiency standards of the finite volume formulation appear to be dependent on the particular case study considering both the issues of simulation time and spatial extent.

Acknowledgments
The research is supported by the UK Engineering and Physical Sciences Research Council (grant ID: EP/K031023/1) and the Chinese Key Project for the Strategic Science Plan in IGSNRR, CAS (grant ID: 2012ZD003). The authors wish to thank Christopher Keylock for proofreading the paper and for his valuable comments, which led to a significant improvement in the quality of the paper. Quihua Liang is also thanked for providing the data of the Thamesmead case study. The present work was partially developed within the framework of the Panta Rhei Research Initiative of the International Association of Hydrological Sciences.

References

Almeida, G. A. M., and P. Bates (2013), Applicability of the local inertial approximation of the shallow water equations to flood modeling, *Water Resour. Res.*, *49*, 4833–4844, doi:10.1002/wrcr.20366.

Araud, Q., P. Finaud, V. Guyot, R. Mosé, and J. Vazquez (2012), An eigenvector-based linear reconstruction approach for time stepping in discontinuous Galerkin scheme used to solve shallow water equations, *Int. J. Numer. Methods Fluids*, *70*(12), 1590–1604.

Audusse, E., F. Bouchut, M. O. Bristeau, R. Klein, and B. Perthame (2004), A fast and stable well-balanced scheme with hydrostatic reconstruction for shallow water flows, *SIAM J. Sci. Comput.*, *25*(6), 2050–2065.

Aureli, F., A. Maranzoni, P. Mignosa, and C. A. Ziveri (2008), A weighted surface-depth gradient method for the numerical integration of the 2D shallow water equations with topography, *Adv. Water Res.*, *31*(7), 962–974.

Benkhaldoun, F., I. Elmahi, and M. Seaid (2010), A new finite volume method for flux gradient and source-term balancing in shallow water equations, *Comput. Methods Appl. Mech. Eng.*, *199*(49-52), 3324–3335.

Bokhove, O. (2005), Flooding and drying in discontinuous Galerkin finite element method for shallow water flows, *J. Sci. Comput.*, *22-23*(1), 47–82.

Bradford, S. F., and B. F. Sanders (2002), Finite volume model for shallow water flooding of arbitrary topography, *J. Hydraul. Eng.*, *128*(3), 289–298.

Caleffi, V., A. Valiani, and A. Bernini (2007), Fourth-order balanced source term treatment in central WENO schemes for shallow water equations, *J. Comput. Phys.*, *218*(1), 228–245.

Cockburn, B., and C. W. Shu (2001), Runge–Kutta discontinuous Galerkin methods for convection-dominated problems, *J. Sci. Comput.*, *16*(3), 173–261.

Crossley A., R. Lamb, S. Walker, and P. Dunning (2010), Fast 2D flood modelling using GPU technology—Recent applications and new developments, paper presented at EGU General Assembly 2010, Vienna, 2–7 May.

Ern, A., S. Piperno, and K. Djadel (2008), A well-balanced Runge–Kutta discontinuous Galerkin method for the shallow-water equations with flooding and drying, *Int. J. Numer. Methods Fluids*, *58*(1), 1–25.

Gallegos, H. A., J. E. Schubert, and B. F. Sanders (2009), Two-dimensional, high-resolution modeling of urban dam-break flooding: A case study of Baldwin Hills, California, *Adv. Water Res.*, *32*(8), 1323–1335.

George, D. L., and R. J. LeVeque (2006), Finite volume methods and adaptive refinement for global tsunami propagation and local inundation, *Sci. Tsunami Hazards*, *24*(5), 319–328.

Godunov, S. K. (1959), A Difference scheme for numerical solution of discontinuous solution of hydrodynamic equations, *Math. Sbornik*, *47-89*(3), 271–306.

Gourgue, O., R. Comblen, J. Lambrechts, T. Karna, V. Legat, and E. Deleersnijder (2009), A flux limiting wetting–drying for finite element shallow-water models, with application to Scheldt Estuary, *Adv. Water Res.*, *32*(12), 1726–1739.

Guan, M., N. G. Wright, and P. A. Sleigh (2013), A robust 2D shallow water model for solving flow over complex topography using Homogenous flux method, *Int. J. Numer. Methods Fluids*, *73*(3), 225–249.

Guinot, V. (2003), *Godunov-Type Schemes: An Introduction for Engineers*, Elsevier, Amsterdam.

Hou, J., Q. Liang, F. Simons, and R. Hinkelmann (2013), A stable 2D unstructured shallow flow model for simulations of wetting and drying over rough terrains, *Comput. Fluids*, *82*, 132–147.

Kesserwani, G. (2013), Topography discretization techniques for Godunov-type shallow water numerical models: A comparative study, *J. Hydraul. Res.*, *51*(4), 351–367.

Kesserwani, G., and Q. Liang (2010), A discontinuous Galerkin algorithm for the two-dimensional shallow water equations, *Comput. Methods Appl. Mech. Eng.*, *199*(49-52), 3356–3368.

Kesserwani, G., and Q. Liang (2011), A conservative high-order discontinuous Galerkin method for the shallow water equations with arbitrary topography, *Int. J. Numer. Methods Eng.*, *86*(1), 47–69.

Kesserwani, G., and Q. Liang (2012a), Locally limited and fully conserved RKDG2 shallow water solutions with wetting and drying, *J. Sci. Comput.*, *50*(1), 120–144.

Kesserwani, G., and Q. Liang (2012b), Dynamically adaptive grid based discontinuous Galerkin shallow water model, *Adv. Water Resour.*, *37*, 23–39.

Krivodonova, L., J. Xin, J. F. Remacle, N. Chevaugeon, and J. E. Flaherty (2004), Shock detection and limiting with discontinuous Galerkin methods for hyperbolic conservation laws, *Appl. Numer. Math.*, *48*(3-4), 323–338.

Kubatko, E. J., J. J. Westerink, and C. Dawson (2006), Hp Discontinuous Galerkin methods for advection dominated problems in shallow water flow, *Comput. Methods Appl. Mech. Eng.*, *96*(1-3), 437–451.

LeFloch, P. G., and M. D. Tanh (2011), A Godunov-type method for the shallow water equations with discontinuous topography in the resonant regime, *J. Comput. Phys.*, *230*(20), 7631–7660.

Lhomme, J., J. Gutierrez-Andres, A. Weisgerber, M. Davison, M. Mulet-Marti, A. Cooper, and B. Gouldby (2010), Testing a new two-dimensional flood modelling system: Analytical tests and application to a flood event, *J. Flood Risk Manage.*, *3*(1), 33–51.

Li, S., and C. J. Duffy (2011), Fully coupled approach to modeling shallow water flow, sediment transport, and bed evolution in rivers, *Water Resour. Res.*, *47*, W03508, doi:10.1029/2010WR009751.

Li, W., H. J. Vriend, Z. Wang, and. D. S. Maren (2013), Morphological modeling using a fully coupled, TVD upwind-biased centered scheme, *Water Resour. Res.*, *49*, 3547–3565, doi:10.1002/wrcr.20138.

Liang, Q. (2010), Flood simulation using a well-balanced shallow flow model, *J. Hydraul. Eng.*, *136*(9), 669–675.

Liang, Q., and F. Marche (2009), Numerical resolution of well-balanced shallow water equations with complex source terms, *Adv. Water Resour.*, *32*(6), 873–884.

Morales-Hernández, M., J. Murillo, and P. García-Navarro (2013), The formulation of internal boundary conditions in unsteady 2-D shallow water flows: Application to flood regulation, *Water Resour. Res.*, *49*, 471–487, doi:10.1002/wrcr.20062.

Mungkasi, S., and S. G. Roberts (2010), On the best quantity reconstructions for a well-balanced finite volume method used to solve the shallow water wave equations with a wet/dry interface, *ANZIAM J.*, *51*(EMAC2009), C48–C65.

Murillo, J., and P. García-Navarro (2012), Wave Riemann description of friction terms in unsteady shallow flows: Application to water and mud/debris floods, *J. Comput. Phys.*, *231*(4), 1963–2001.

Neal, J., I. Villanueva, N. Wright, T. Willis, T. Fewtrell, and P. Bates (2012), How much physical complexity is needed to model flood inundation?, *Hydrol. Processes*, *26*(15), 2264–2282.

Néelz, S., and G. Pender (2013), Benchmarking the latest generation of 2D hydraulic modelling packages, *UK Environ. Agency Sci. Rep. SC120002*. [Available at http://evidence.environment-agency.gov.uk/FCERM/Libraries/FCERM_Project_Documents/SC120002_Benchmarking_2D_hydraulic_models_Report.sflb.ashx.]

Nikolos, I. K., and A. I. Delis (2009), An unstructured node-centred finite volume scheme for shallow water flows with wet/dry fronts over complex topography, *Comput. Methods Appl. Mech. Eng.*, *189*(47–48), 3723–3750.

Ozmen-Cagatay, H., and S. Kocaman (2011), Dam-break flow in the presence of obstacle: Experiment and CDF simulation, *Eng. Appl. Comput. Fluid Mech.*, *5*(4), 541–552.

Sanders, B. F., and S. F. Bradford (2006), Impact of limiters on accuracy of high-resolution flow and transport models, *J. Eng. Mech.*, *132*(1), 87–98.

Sanders, B. F., J. E. Schubert, and R. L. Detwiler (2010), ParBreZo: A parallel, unstructured grid, Godunov-type, shallow-water code for high-resolution flood inundation modeling at the regional scale, *Adv. Water Resour.*, *33*(12), 1456–1467.

Soares Frazao, S., and G. Testa (1999), The Toce River test case: Numerical results analysis, paper presented at 3rd CADAM workshop, Milan, Italy.

Thacker, W. C. (1981), Some exact solutions to the nonlinear shallow water equations, *J. Fluid Mech.*, *107*, 499–508.

Toro, E. F. (2001), *Shock-Capturing Methods for Free-Surface Shallow Flows*, John Wiley, N. Y.

Toro, E. F., and P. García-Navarro, (2007), Godunov-type methods for free-surface shallow flows: A review, *J. Hydraul. Res.*, *45*(6), 737–751.

Van Leer, B. (1979), Towards the ultimate conservative difference scheme, V. A second order sequel to Godunov's method, *J. Comput. Phys.*, *32*(1), 101–136.

Volp, N. D., B. C. van Prooijen, and G. S. Stelling (2013), A finite volume approach for shallow water flow accounting for high-resolution bathymetry and roughness data, *Water Resour. Res.*, *49*, 4126–4135, doi:10.1002/wrcr.20324.

Wang, Y., Q. Liang, G. Kesserwani, and J. W. Hall (2011), A 2D shallow flow model for practical dam-break simulations, *J. Hydraul. Res.*, *49*(3), 307–316.

Xing, Y., X. Zhang, and C. W. Shu (2010), Positivity preserving high-order well-balanced discontinuous Galerkin methods for the shallow water equations, *Adv. Water Resour.*, *33*(12), 1476–1493.

Zhou, T., Y. Li, and C. W. Shu (2001), Numerical comparison of WENO finite volume and Runge–Kutta discontinuous Galerkin methods, *J. Sci. Comput.*, *16*(2), 145–171.